



Cite this: *RSC Adv.*, 2021, **11**, 17032

# Synthesis of $\text{TiO}_2\text{--Ag}_3\text{PO}_4$ photocatalyst material with high adsorption capacity and photocatalytic activity: application in the removal of dyes and pesticides

Emmanuel Nyankson, Johnson K. Efavi, \* Benjamin Agyei-Tuffour and Gloria Manu

The photocatalytic activity of  $\text{TiO}_2$  can be enhanced by coupling it with other semiconductors and the semiconductor composites may find useful application in water treatment technologies.  $\text{TiO}_2\text{--Ag}_3\text{PO}_4$  composites were synthesized and characterized with XRD, SEM-EDX and DRS. The synthesized  $\text{TiO}_2\text{--Ag}_3\text{PO}_4$  showed high photocatalytic activity in the presence UV-vis light on rhodamine B, methylene blue and the pesticides imidacloprid, atrazine and pyrimethanil. LC-MS analysis of the photodegraded pyrimethanil led to the identification of hydroxylated and aliphatic derivatives of pyrimethanil. The photocatalytic activity of the coupled semiconductor was higher than that of the bare  $\text{TiO}_2$  and  $\text{Ag}_3\text{PO}_4$  and this was attributed to the unique band matching between  $\text{TiO}_2$  and  $\text{Ag}_3\text{PO}_4$  which resulted in efficient charge separation and subsequent reduction in the electron–hole recombination. In addition, the synthesized  $\text{TiO}_2\text{--Ag}_3\text{PO}_4$  showed strong adsorption for water soluble dyes implying that  $\text{TiO}_2\text{--Ag}_3\text{PO}_4$  can remove pollutants through photocatalysis and adsorption. The results from the study showed the potential application of  $\text{TiO}_2\text{--Ag}_3\text{PO}_4$  composite in water treatment technologies.

Received 17th March 2021  
 Accepted 30th April 2021

DOI: 10.1039/d1ra02128a  
[rsc.li/rsc-advances](http://rsc.li/rsc-advances)

## 1 Introduction

Increased population and industrial activities have resulted in industrial effluent generation and pollution of water bodies, harmful to humans and aquatic life especially when they contain substances such as dyes, pesticides, heavy metals and pharmaceutical wastes.<sup>1</sup>

The world production of dyes has increased dramatically over the past years and these azo dyes, reactive dyes, solvent dyes for instance are used by the textile, food, adhesive, cosmetics, arts, construction, paints, glass and ceramic industries extensively.<sup>2</sup> The release of these colored organic substances into our environment is a source of aesthetic pollution and is detrimental to the environmental ecosystems. In addition, large concentrations of organic dyes in the aquatic environment may be toxic to aquatic species and disulphonated azo dyes has been reported to be a major source of problem in drinking water plants globally.<sup>3</sup>

In addition there is high demand for pesticides globally as a result of increasing agricultural activities and the toxins in the pesticides are leached into surface and ground water sources which are detrimental to human health and aquatic life.<sup>4</sup> The alarming impact of these activities on the environment has

prompted the European Union to set standards under the European Directive 2000/60/EC that establishes maximum concentrations for pesticides and related harmful chemical substances in drinking waters to safeguard its detrimental effects on humans.<sup>5</sup>

High chemical stability and low biodegradability of these organic pollutants have necessitated the search for suitable treatment methods that can easily break down inherent chemical components. Techniques such as adsorption, biodegradation, ozonation and photo-Fenton processes have been adopted in treating dyes and pesticides pollutants.<sup>6</sup> However, these methods have been reported to be ineffective in the treatment of polluted water bodies.<sup>7</sup> Recent studies have been focused on the use of advance oxidation processes such as photocatalysis for the removal of dyes and pesticides from wastewaters,<sup>8</sup> degradation of crude oil fractions,<sup>9</sup> and for aquatic disinfection.<sup>10</sup>

Photocatalysis involves the generation of reactive oxygen species (ROS) in the presence of sunlight, semiconductor, dissolved oxygen and water. These ROS are able to oxidize and mineralize organic contaminants into carbon dioxide and inorganic anions.<sup>11</sup> Hence, semiconductor based photocatalysts have received enormous attention because of their potential in solving some of the most challenging environmental problems. One of the most widely investigated photocatalyst is  $\text{TiO}_2$ . Though  $\text{TiO}_2$  is chemically stable, its wide band gap energy limits its efficient utilization in sunlight irradiation. That is  $\text{TiO}_2$  is active in the UV region of the electromagnetic spectrum

Department of Materials Science and Engineering, University of Ghana, LG 77, Accra, Ghana. E-mail: [jkefavi@ug.edu.gh](mailto:jkefavi@ug.edu.gh)



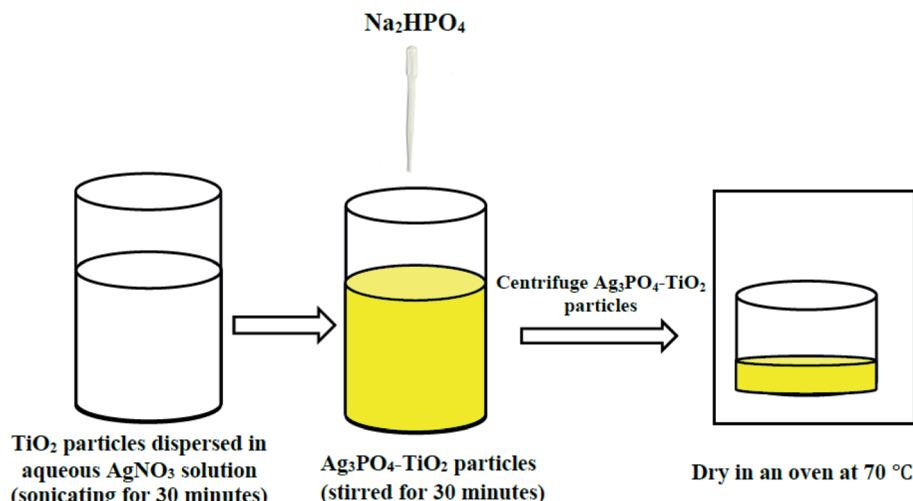


Fig. 1 Synthesis scheme of the  $\text{Ag}_3\text{PO}_4$ - $\text{TiO}_2$  nanocomposite.

which makes up only *ca.* 4–5% of the electromagnetic spectrum and this limits its practical application. Developing semiconductor materials that are very sensitive to visible light and can be effectively utilized in practical applications has become the focus of many researchers. Different visible light active photocatalysts such as  $\text{Au}/\text{TiO}_2$ ,<sup>12</sup>  $\text{C}-\text{TiO}_2/\text{g-C}_3\text{N}_4$ ,<sup>13</sup>  $\text{YFeO}_3$ ,<sup>14</sup> defect  $\text{ZnO}$  nanorods<sup>15</sup> and  $\text{ZnO}/\text{CuO}$ <sup>16</sup> have been developed by researchers. These semiconductor photocatalyst may be decorated with bimetallic nanoparticle cocatalyst to enhance their degradation efficiency.<sup>17</sup> In addition, 3D graphene based photocatalyst have been developed and utilized in environmental pollutant degradation.<sup>18</sup>  $\text{Ag}_3\text{PO}_4$  with extremely high visible light photocatalytic activity has also been reported.<sup>19</sup>

Photocorrosion which involves the conversion of  $\text{Ag}^+$  to  $\text{Ag}^0$  in the absence of an electron acceptor has been reported as a major drawback of  $\text{Ag}_3\text{PO}_4$  photocatalyst. This occurs as a result of the solubility of  $\text{Ag}_3\text{PO}_4$  in aqueous solution.<sup>19a,20</sup> In addition to using  $\text{Ag}_3\text{PO}_4$  as a stand-alone photocatalyst, several composite photocatalyst have been developed by combining  $\text{Ag}_3\text{PO}_4$  with  $\text{AgI}$ ,<sup>21</sup>  $\text{g-C}_3\text{N}_4$ ,<sup>22</sup> carbon quantum dots,<sup>23</sup>  $\text{SrTiO}_3$  (ref. 24) and  $\text{TiO}_2$ .<sup>25</sup>  $\text{TiO}_2$ - $\text{Ag}_3\text{PO}_4$  has been reported to be the most efficient among the

composite photocatalyst formed with  $\text{Ag}_3\text{PO}_4$ .<sup>26</sup> A photocatalytic system made up of carbon fiber cloth as a porous substrate and  $\text{Ag}_3\text{PO}_4$ / $\text{TiO}_2$  as a photocatalyst with a rhodamine B dye removal efficiency of  $\sim 99.5\%$  has been reported.<sup>27</sup> Graphene oxide (GO) embedded ternary heterostructure nanocomposites of  $\text{N}-\text{TiO}_2$ / $\text{Ag}_3\text{PO}_4$ @GO with different weight ratios of  $\text{N}-\text{TiO}_2$  to  $\text{Ag}_3\text{PO}_4$  has also been developed.<sup>28</sup> It should however be mentioned that, to the best of the authors knowledge, efficiency of all the reported  $\text{TiO}_2$ - $\text{Ag}_3\text{PO}_4$  photocatalyst was examined using water soluble dyes and phenols,<sup>29</sup> and none of the articles reported a detailed adsorption kinetics and equilibrium studies. A detailed adsorption equilibrium and kinetic studies is required to understand the adsorption mechanism of  $\text{Ag}_3\text{PO}_4$ - $\text{TiO}_2$  towards organic molecules.<sup>30</sup>

In this study, a one pot method was used to synthesize  $\text{Ag}_3\text{PO}_4$ - $\text{TiO}_2$  photocatalyst. The synthesized photocatalyst was characterized with XRD, SEM-EDX, and DRS. The photodegradation efficiency was examined using rhodamine B dye, methylene blue dye and three pesticides; atrazine, imidacloprid and pyrimethanil. Detailed adsorption kinetic and equilibrium studies was conducted on the  $\text{Ag}_3\text{PO}_4$ - $\text{TiO}_2$  using methylene blue dye. The

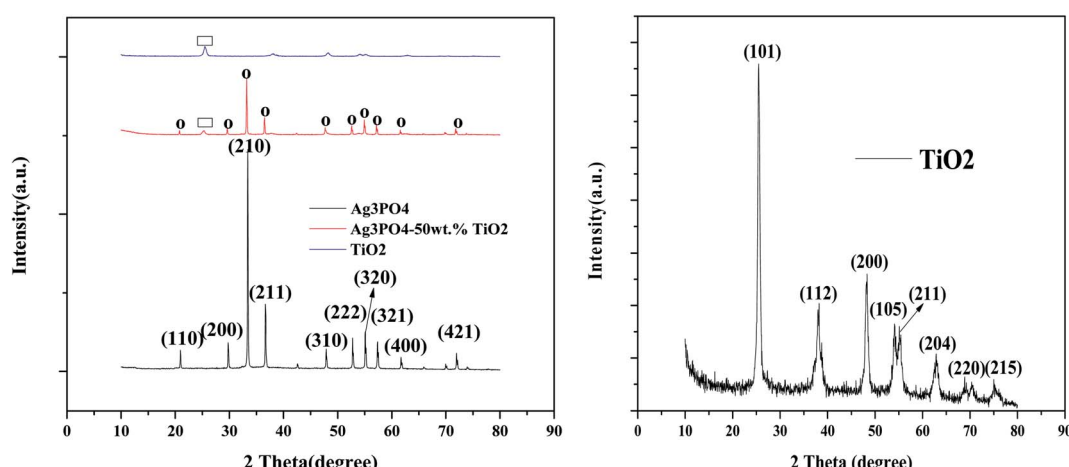


Fig. 2 XRD patterns for (A)  $\text{Ag}_3\text{PO}_4$ ,  $\text{TiO}_2$  and  $\text{Ag}_3\text{PO}_4$ -50 wt%  $\text{TiO}_2$ , (B) enlarged XRD pattern for  $\text{TiO}_2$  [ $\text{O} = \text{Ag}_3\text{PO}_4$ ,  $\square = \text{TiO}_2$ ].



photodegradation by-products obtained after subjecting pyrimethanil to photocatalysis were identified using LC-MS.

## 2 Experimental procedure

### 2.1 Materials

All chemical reagents used in this study were analytical grade and were purchased from Sigma Aldrich, U.K. The chemical reagents were used without further purification. Deionized water was used throughout this study.

### 2.2 Synthesis of $\text{Ag}_3\text{PO}_4$ - $\text{TiO}_2$ nanocomposite

In a typical synthesis, a calculated amount of  $\text{TiO}_2$  (P25) was dispersed in 150 mL of 0.02 M  $\text{AgNO}_3$  by sonication for 30 minutes. 122.5 mL of 0.2 M  $\text{Na}_2\text{HPO}_4$  was then added dropwise while stirring. The resulting bright yellow solution was continuously stirred

for 30 minutes and then centrifuged to collect the bright yellow precipitate. The collected precipitate was washed repeatedly (three cycles) with deionized water and dried at 70 °C to obtain  $\text{Ag}_3\text{PO}_4$ - $\text{TiO}_2$  nanocomposite. Different amounts of  $\text{TiO}_2$  were used in the synthesis to obtain samples with 10 wt%, 25 wt%, 50 wt% and 75 wt%  $\text{TiO}_2$ . A similar procedure was used to obtain  $\text{Ag}_3\text{PO}_4$  but without the addition of  $\text{TiO}_2$ . The synthesis scheme of the  $\text{Ag}_3\text{PO}_4$ - $\text{TiO}_2$  nanocomposite is provided in Fig. 1 below.

### 2.3 Product characterization

**2.3.1 X-ray diffraction (XRD).** The X-ray diffraction patterns were obtained with Bruker D8 advanced focus diffractometer fitted with position sensitive detector (LynxEye) and standard detector.  $\text{Cu-K}\alpha$  radiation ( $\lambda = 0.15405$  nm) and a 2theta angular range of 10–80° were used.

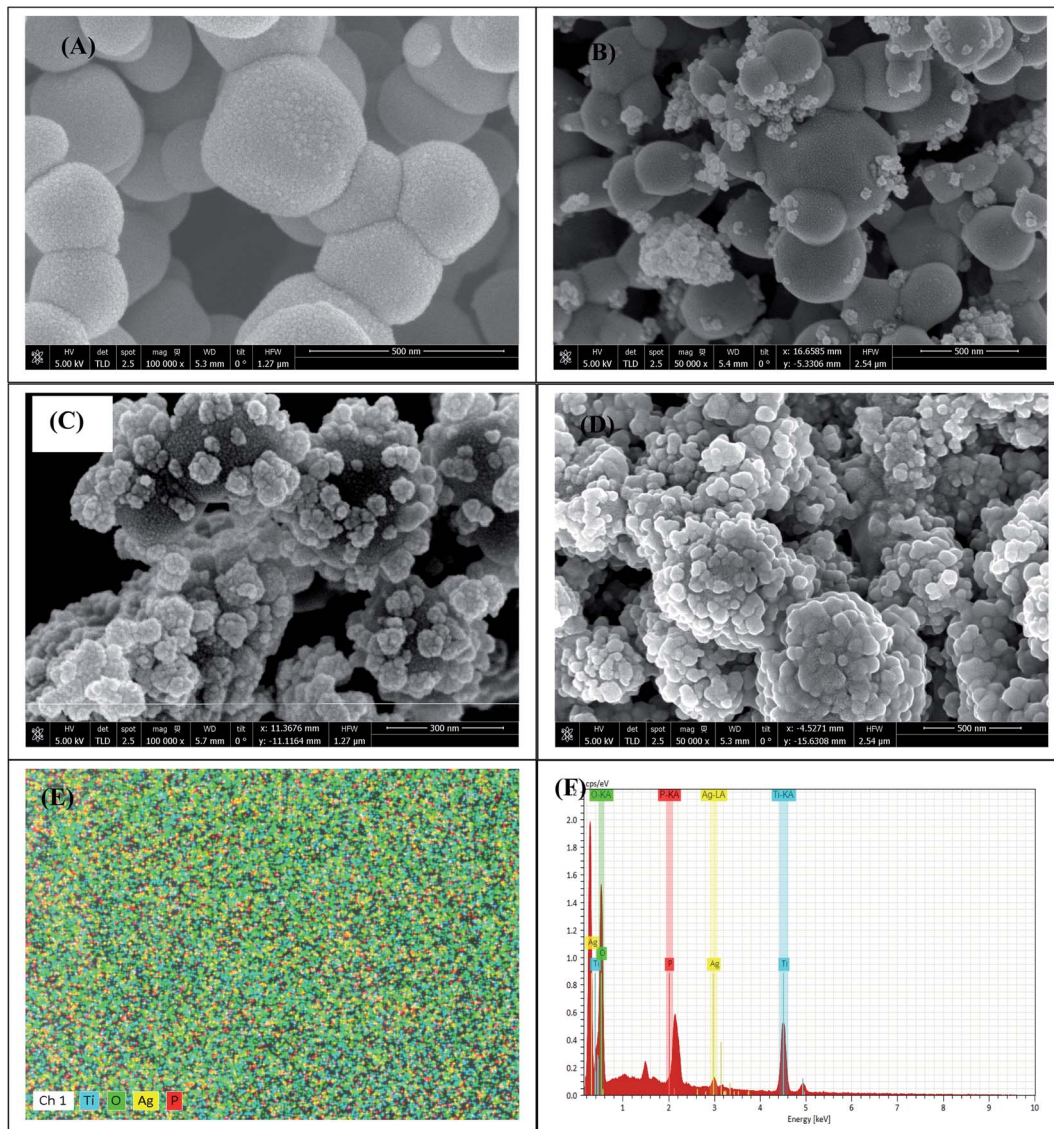


Fig. 3 SEM images (A)  $\text{Ag}_3\text{PO}_4$ , (B)  $\text{Ag}_3\text{PO}_4$ -25 wt%  $\text{TiO}_2$ , (C)  $\text{Ag}_3\text{PO}_4$ -50 wt%  $\text{TiO}_2$  and (D)  $\text{Ag}_3\text{PO}_4$ -75 wt%  $\text{TiO}_2$ ; (E) EDX mapping for  $\text{Ag}_3\text{PO}_4$ -50 wt%  $\text{TiO}_2$ , (F) EDX spectrum for  $\text{Ag}_3\text{PO}_4$ -50 wt%  $\text{TiO}_2$ .



**2.3.2 Scanning electron microscopy/energy-dispersive X-ray spectroscopy.** The morphology of the synthesized nanocomposites was examined with scanning electron microscopy (FEI Nova NanoSEM) connected to EDX acquisition detector. The elemental composition was determined through EDX.

**2.3.3 Diffuse reflectance spectroscopy (DRS).** DRS was conducted using Ocean Optics USB-4000 spectrometer with a dedicated reflectance probe. Illumination was supplied with a Deuterium/Halogen source across the UV-VIS range. The synthesized nanocomposites are compressed into a flat film between glass microscope slides prior to measurement and a commercial PTFE reflectance standard was used as reflectance calibration.

**2.3.4 Adsorption studies.** The adsorption capability of the synthesized nanocomposite was examined using methylene blue dye. 100 mg of  $\text{Ag}_3\text{PO}_4$ - $\text{TiO}_2$  was added to 200 mL aqueous solution of methylene blue ( $5 \text{ mg L}^{-1}$ ). Aliquots of the methylene blue solution were taken at specified time intervals. The sampled solution was centrifuged at 6000 rpm for 5 minutes to remove the powdered nanocomposite. The concentration of methylene blue was obtained by measuring the absorbance at 655 nm wavelength using Ocean Optics 4000 USB modular UV-VIS spectrometer.

**2.3.5 Photocatalytic methylene blue, rhodamine blue and pesticide degradation.** The photocatalytic activity of the synthesized  $\text{Ag}_3\text{PO}_4$ - $\text{TiO}_2$  was examined using rhodamine B ( $6 \text{ mg L}^{-1}$ ) and methylene blue ( $8 \text{ mg L}^{-1}$ ) dyes and pesticides (pyrimethanil, imidacloprid and atrazine). In a typical photocatalytic degradation of rhodamine B dye, 200 mL of rhodamine B solution in deionized water was used with a photocatalyst suspension concentration of  $0.5 \text{ g L}^{-1}$ . A jacketed glass reactor with a quartz tube immersion well was used with illumination from 300 W Tungsten Halogen lamp. For each of the experiments, the solution was stirred in the dark for 30 minutes (24 hours for pesticide solutions) to attain an adsorption-desorption equilibrium for illumination. 2 mL aliquots were taken at specific time intervals and centrifuged at 6000 rpm for 5 minutes to remove the powdered photocatalyst. The dye concentration was quantified using Ocean Optics 4000 USB modular UV-vis spectrometer with an absorbance values taken at 554 nm. A similar procedure was used for the photocatalytic degradation of the methylene blue and pesticides. However, the absorbance values were taken at 665 nm for methylene blue, 269 nm (pyrimethanil), 270 nm (imidacloprid), and 222 nm (atrazine). The degraded pesticide solution obtained from pyrimethanil was analyzed with LC-MS to identify photodegraded products.

### 3 Results and discussion

#### 3.1 Characterization of $\text{Ag}_3\text{PO}_4$ - $\text{TiO}_2$

The XRD patterns of the pristine P25  $\text{TiO}_2$ ,  $\text{Ag}_3\text{PO}_4$ , and  $\text{Ag}_3\text{PO}_4$ -50 wt%  $\text{TiO}_2$  are presented in Fig. 2. The XRD pattern for the  $\text{Ag}_3\text{PO}_4$  showed well defined crystalline  $\text{Ag}_3\text{PO}_4$  with sharp and intense diffraction peaks that can be indexed to the body-centered crystal structure (JCPDS no. 06-0505).

The dominant peaks at  $33.4^\circ$  and  $36.6^\circ$  correspond to the (210) and (211) crystallographic planes,<sup>31</sup> respectively. On the other hand,  $\text{TiO}_2$  showed an intense peak at  $25.5^\circ$  which represents the (101) crystallographic plane and can be

indexed to the anatase phase (JCPDS no. 21-1272). With the “rectangles” representing the anatase phase present in  $\text{TiO}_2$  and the circles representing the cubic structure of  $\text{Ag}_3\text{PO}_4$ , the prepared  $\text{Ag}_3\text{PO}_4$ - $\text{TiO}_2$  composite has all the crystallographic planes present in the crystalline cubic structure of  $\text{Ag}_3\text{PO}_4$  and the (101) plane of the anatase phase of  $\text{TiO}_2$ . The as-prepared  $\text{Ag}_3\text{PO}_4$ - $\text{TiO}_2$  is therefore expected to exhibit high photocatalytic activity. Though the  $\text{Ag}_3\text{PO}_4$ - $\text{TiO}_2$  used for the analysis contained 50 wt%  $\text{TiO}_2$ , the diffraction peaks of the  $\text{TiO}_2$  is weak. This can be ascribed to the relatively low crystallinity of  $\text{TiO}_2$  when compared with that of  $\text{Ag}_3\text{PO}_4$ .

The morphology of the synthesized  $\text{Ag}_3\text{PO}_4$  and  $\text{Ag}_3\text{PO}_4$ - $\text{TiO}_2$  photocatalyst were examined with SEM and the images presented in Fig. 3. The pristine  $\text{Ag}_3\text{PO}_4$  is irregularly shaped spherical particles with diameter of *ca.* 100–400 nm. The P25 used for this study has a much smaller diameter of *ca.* 20 nm. The SEM images showed the agglomeration of the  $\text{TiO}_2$  particles. The particle sizes of the  $\text{Ag}_3\text{PO}_4$  and  $\text{TiO}_2$  in the  $\text{Ag}_3\text{PO}_4$ - $\text{TiO}_2$  composite (Fig. 3 B–D) is similar to the pure  $\text{Ag}_3\text{PO}_4$  and  $\text{TiO}_2$ . It can be seen from Fig. 3B to D that the  $\text{TiO}_2$  covered the surface of the  $\text{Ag}_3\text{PO}_4$  creating a heterojunction. The extent of the surface coverage is dependent on the wt% of the  $\text{TiO}_2$  used for the synthesis. This coverage is expected to influence the photocatalytic activity. Positively charged ions adsorbs strongly to the surface of  $\text{TiO}_2$ .<sup>29a,32</sup> Since the P25  $\text{TiO}_2$  was first dispersed in  $\text{AgNO}_3$ , the  $\text{Ag}^+$  ions adsorbed onto the surface of the  $\text{TiO}_2$ . The reaction between the  $\text{Ag}^+$  and the  $\text{PO}_4^{3-}$  occurred on the surface of the  $\text{TiO}_2$  when the  $\text{Na}_2\text{HPO}_4$  was added, resulting in the formation of the  $\text{TiO}_2$ - $\text{Ag}_3\text{PO}_4$  composite. The SEM-EDX (Fig. 3E and F) spectrum confirms the presence of Ti, O, Ag and P. The elemental mapping showed that the elements Ti and O were evenly distributed on the surface of the  $\text{Ag}_3\text{PO}_4$ .

The UV-vis diffused reflectance spectra of the product with different wt% of  $\text{TiO}_2$  are shown in Fig. 4. The P25  $\text{TiO}_2$  only absorbs light in the UV region of the electromagnetic spectrum with wavelength lower than approximately 390 nm. On the other hand, the pure  $\text{Ag}_3\text{PO}_4$  has intense light absorption in the

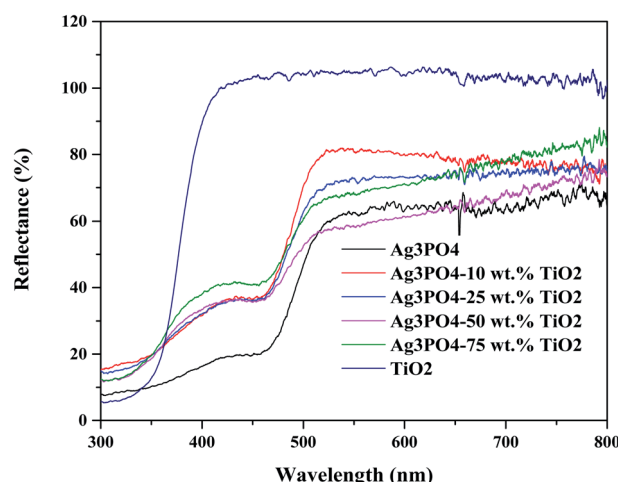


Fig. 4 UV-vis DRS spectra of  $\text{Ag}_3\text{PO}_4$ ,  $\text{TiO}_2$  and the various formulations of  $\text{Ag}_3\text{PO}_4$ - $\text{TiO}_2$ .



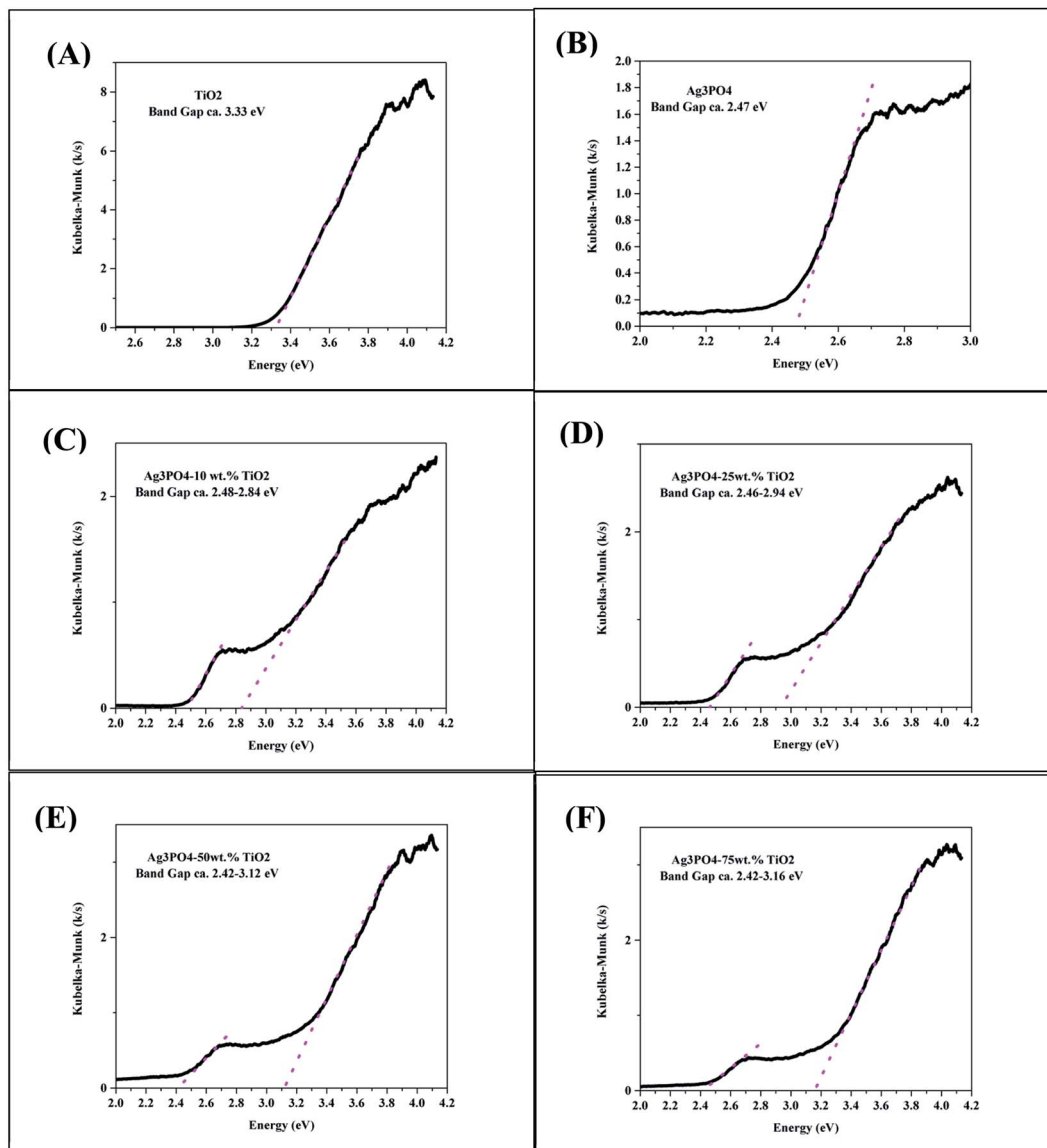


Fig. 5 Optical band gap estimation using Kubelka–Munk model for (A)  $\text{TiO}_2$ , (B)  $\text{Ag}_3\text{PO}_4$ , (C)  $\text{Ag}_3\text{PO}_4$ –10 wt%  $\text{TiO}_2$ , (D)  $\text{Ag}_3\text{PO}_4$ –25 wt%  $\text{TiO}_2$ , (E)  $\text{Ag}_3\text{PO}_4$ –50 wt%  $\text{TiO}_2$  and (F)  $\text{Ag}_3\text{PO}_4$ –75 wt%  $\text{TiO}_2$ .

visible light region of the electromagnetic spectrum. The shape of the DRS spectra of the composite is a combination of that of  $\text{Ag}_3\text{PO}_4$  and  $\text{TiO}_2$  further proving the absence of any chemical interaction between  $\text{TiO}_2$  and  $\text{Ag}_3\text{PO}_4$ . This agrees with observation made by Taheri *et al.*<sup>33</sup> The composite  $\text{Ag}_3\text{PO}_4$ – $\text{TiO}_2$  showed strong absorption in the visible light region due to the excellent visible light absorption by  $\text{Ag}_3\text{PO}_4$ . The composite  $\text{Ag}_3\text{PO}_4$ – $\text{TiO}_2$  can therefore harvest more visible light and result in an improved photocatalytic activity. The optical band gap of the photocatalysts synthesized were estimated from the DRS spectra using the Kubelka–Munk model<sup>34</sup> and are presented in Fig. 5. The optical band gap of the  $\text{TiO}_2$  and  $\text{Ag}_3\text{PO}_4$  were estimated to be 3.33 and 2.47 eV, respectively. The composite samples are characterized by two absorption thresholds, one corresponding to the  $\text{TiO}_2$  and the other,  $\text{Ag}_3\text{PO}_4$ . A slight variation in the two absorption thresholds were observed upon

varying the weight percent of the  $\text{TiO}_2$  used for the synthesis. The band gap for the absorption threshold corresponding to  $\text{TiO}_2$  decreased with decreasing wt% of  $\text{TiO}_2$  in the  $\text{TiO}_2$ – $\text{Ag}_3\text{PO}_4$  composite as can be seen in Fig. 5.

### 3.2 Photodegradation of rhodamine B, methylene blue and pesticides

Fig. 6A shows the photocatalytic performance of rhodamine B solution (200 mL, 6 mg L<sup>–1</sup>) over  $\text{Ag}_3\text{PO}_4$ ,  $\text{TiO}_2$  and  $\text{Ag}_3\text{PO}_4$ – $\text{TiO}_2$  composites at a photocatalyst concentration of 0.5 g L<sup>–1</sup> under UV-vis light irradiation. Before irradiation, the dye–photocatalyst solution was stirred in the dark for 30 minutes to achieve adsorption–desorption equilibrium. The percentages of rhodamine B adsorbed by  $\text{Ag}_3\text{PO}_4$ ,  $\text{TiO}_2$  and  $\text{Ag}_3\text{PO}_4$ – $\text{TiO}_2$  composite were 14.5, 18.8 and 12.0 wt%, respectively. The wt%



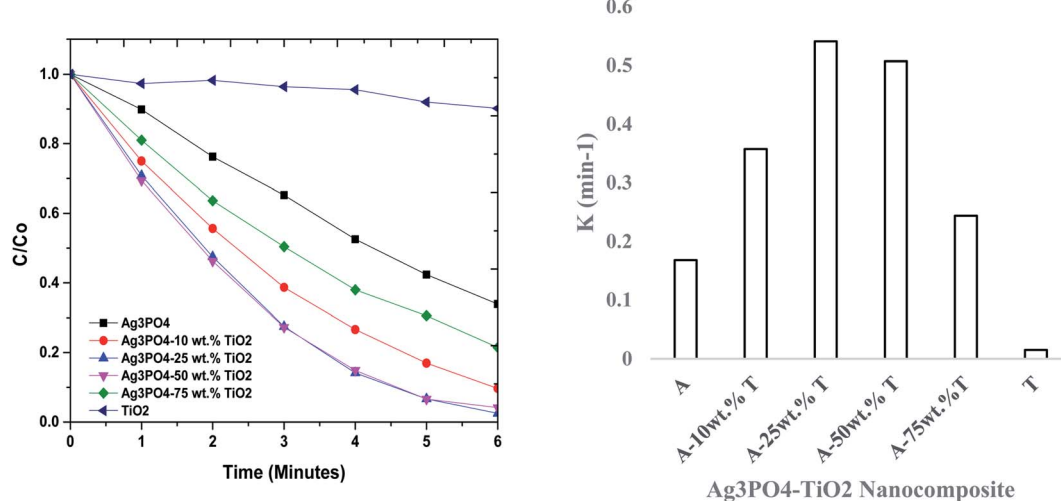


Fig. 6 (A) Photocatalytic activities of  $\text{Ag}_3\text{PO}_4$ ,  $\text{TiO}_2$  and  $\text{Ag}_3\text{PO}_4$ - $\text{TiO}_2$  (10, 25, 50, and 75 wt% of  $\text{TiO}_2$ ) and (B) rate constants of  $\text{Ag}_3\text{PO}_4$ (A),  $\text{TiO}_2$ (T) and  $\text{Ag}_3\text{PO}_4$ - $\text{TiO}_2$  (A-wt% T) on  $6 \text{ mg L}^{-1}$  rhodamine B dye.

of the rhodamine B adsorbed by the various formulations of the composite material was *ca.* 12%. The data obtained from the photocatalysis was fitted with a pseudo first order kinetics and the rate constants ( $k$ ) calculated (Fig. 6B). Under UV-vis light irradiation, *ca.* 9.8% of rhodamine B ( $k = 0.0153 \text{ min}^{-1}$ ) was degraded by  $\text{TiO}_2$  within the time (6 min) frame that the photocatalysis analysis was carried out. On the other hand, *ca.* 66% of the rhodamine concentration was degraded by  $\text{Ag}_3\text{PO}_4$  within 6 min ( $k = 0.168 \text{ min}^{-1}$ ). The rate at which the concentration of the dye solution degraded by the composite ( $\text{Ag}_3\text{PO}_4$ - $\text{TiO}_2$ ) decreased was significantly higher than that of  $\text{Ag}_3\text{PO}_4$  and  $\text{TiO}_2$ . For the same time period (6 min), the degradation efficiency obtained from the composites were 90, 98, 96 and 79% for  $\text{Ag}_3\text{PO}_4$ -10 wt%  $\text{TiO}_2$  ( $k = 0.3571 \text{ min}^{-1}$ ),  $\text{Ag}_3\text{PO}_4$ -25 wt%  $\text{TiO}_2$  ( $K = 0.5406 \text{ min}^{-1}$ ),  $\text{Ag}_3\text{PO}_4$ -50 wt%  $\text{TiO}_2$  ( $K = 0.5069 \text{ min}^{-1}$ ) and  $\text{Ag}_3\text{PO}_4$ -75 wt%  $\text{TiO}_2$  ( $K = 0.2438 \text{ min}^{-1}$ ), respectively. These values indicate that  $\text{Ag}_3\text{PO}_4$  and  $\text{TiO}_2$  act

synergistically to enhance photodegradation. This is so because the degradation efficiency and the rate constants of the composite  $\text{Ag}_3\text{PO}_4$ - $\text{TiO}_2$  were significantly higher than that of the individual components. The synergy was highest at 25 wt%  $\text{TiO}_2$ . A similar observation was reported by Taheri *et al.*<sup>33</sup> This observation can be attributed to the formation of a heterojunction between the  $\text{TiO}_2$  and the  $\text{Ag}_3\text{PO}_4$ .<sup>33</sup> In addition, the photocatalytic activity is also affected by the extend of surface coverage. To obtain maximum photocatalytic activity, the extend at which the  $\text{Ag}_3\text{PO}_4$  surface is covered by  $\text{TiO}_2$  should be minimized. The uncovered surface of  $\text{Ag}_3\text{PO}_4$  is utilized for maximum absorption of visible light.

The degradation of methylene blue (200 mL,  $8 \text{ mg L}^{-1}$ , 0.5 g  $\text{L}^{-1}$  catalyst concentration) was also examined under UV-vis light irradiation and the results shown in Fig. 7. After the adsorption-desorption equilibrium was attained, 8.9 ( $\text{Ag}_3\text{PO}_4$ ), 16.7 ( $\text{TiO}_2$ ), 31.0 ( $\text{Ag}_3\text{PO}_4$ -10 wt%  $\text{TiO}_2$ ), 66.4 ( $\text{Ag}_3\text{PO}_4$ -25 wt%

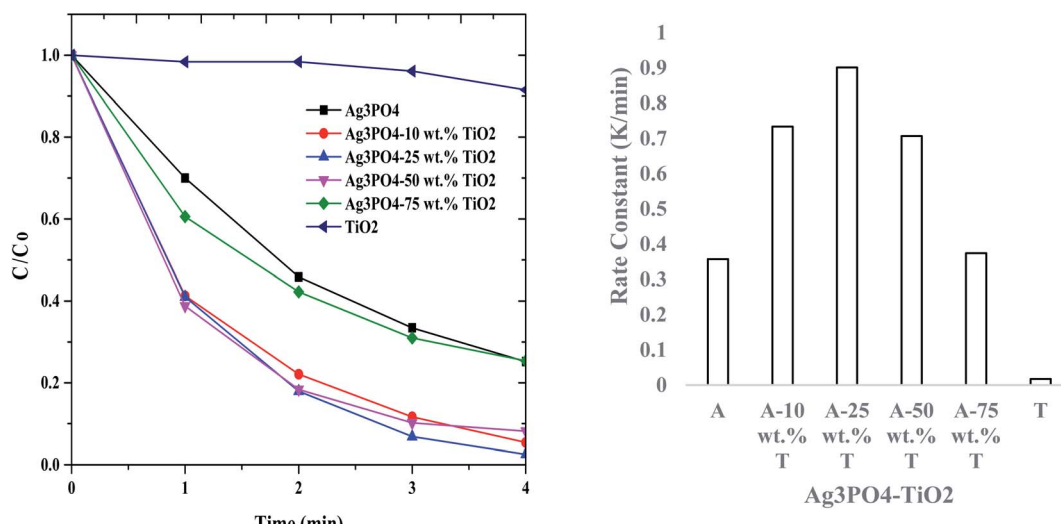


Fig. 7 (A) Photocatalytic activities of  $\text{Ag}_3\text{PO}_4$ ,  $\text{TiO}_2$  and  $\text{Ag}_3\text{PO}_4$ - $\text{TiO}_2$  (10, 25, 50, and 75 wt% of  $\text{TiO}_2$ ) and (B) rate constants of  $\text{Ag}_3\text{PO}_4$ (A),  $\text{TiO}_2$ (T) and  $\text{Ag}_3\text{PO}_4$ - $\text{TiO}_2$  (A-wt% T) on  $8 \text{ mg L}^{-1}$  methylene blue dye.

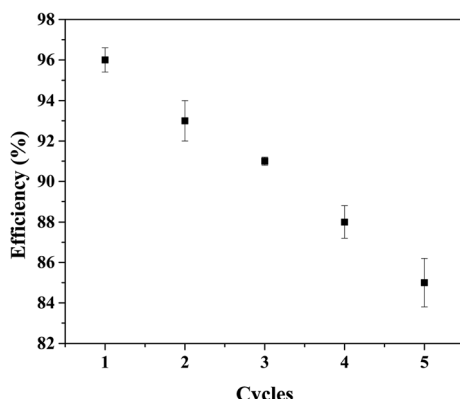


Fig. 8 The reusability of  $\text{Ag}_3\text{PO}_4$ – $\text{TiO}_2$  nanocomposite.

$\text{TiO}_2$ ), 71.8 ( $\text{Ag}_3\text{PO}_4$ -50 wt%  $\text{TiO}_2$ ) and 79.6% ( $\text{Ag}_3\text{PO}_4$ -75 wt%  $\text{TiO}_2$ ) of the methylene blue dye was removed by adsorption. This informed the authors to conduct a detailed adsorption kinetics and equilibrium test. The photocatalytic activity of  $\text{TiO}_2$  on methylene blue was low (16.7%,  $k = 0.0175 \text{ min}^{-1}$  within 4 min). Within the same time frame,  $\text{Ag}_3\text{PO}_4$  recorded a photocatalytic efficiency of 79% with a rate constant of  $0.3573 \text{ min}^{-1}$ . From Fig. 7, it is observed that the  $\text{Ag}_3\text{PO}_4$ – $\text{TiO}_2$  composite is much more active photocatalytically than  $\text{Ag}_3\text{PO}_4$  and  $\text{TiO}_2$ . The photocatalytic efficiency and the rate constants were 96.3% and

$0.7338 \text{ min}^{-1}$ , 99.1% and  $0.9010 \text{ min}^{-1}$ , 97.7% and  $0.7069 \text{ min}^{-1}$  and, 94.8% and  $0.3743 \text{ min}^{-1}$ , for  $\text{Ag}_3\text{PO}_4$ -10 wt%  $\text{TiO}_2$ ,  $\text{Ag}_3\text{PO}_4$ -25 wt%  $\text{TiO}_2$ ,  $\text{Ag}_3\text{PO}_4$ -50 wt%  $\text{TiO}_2$  and  $\text{Ag}_3\text{PO}_4$ -75 wt%  $\text{TiO}_2$ , respectively. Again, the  $\text{Ag}_3\text{PO}_4$ -25 wt%  $\text{TiO}_2$  recorded the highest photocatalytic efficiency and rate constant.

The stability of the synthesized nanocomposite was examined using  $\text{Ag}_3\text{PO}_4$ -50 wt%  $\text{TiO}_2$  and rhodamine B. The results for the stability/reusability of the nanocomposite is presented in Fig. 8. After five cycles of the photodegradation test, the degradation efficiency decreased from 96% to 85%. The developed  $\text{Ag}_3\text{PO}_4$ – $\text{TiO}_2$  nanocomposite is therefore fairly stable under the experimental conditions used in this study.

The photocatalytic activity of  $\text{Ag}_3\text{PO}_4$ -25 wt%  $\text{TiO}_2$  on three pesticides (pyrimethanil, atrazine and imidacloprid) was examined (Fig. 9). The UV-vis absorption spectrum in Fig. 9 indicated a reduction in the concentration of the pesticides after photocatalysis. Though the concentration of the three pesticides are the same, the rate of degradation differed from one pesticide to the other. The pseudo first order rate constants were calculated to be 1.319, 0.013 and 0.011  $\text{min}^{-1}$  for pyrimethanil, imidacloprid and atrazine, respectively. The variation in the calculated rate constants can be attributed to the different stabilities of the pesticides used for this study. The photoproducts formed from the photodegradation of pyrimethanil were identified with LC-MS.

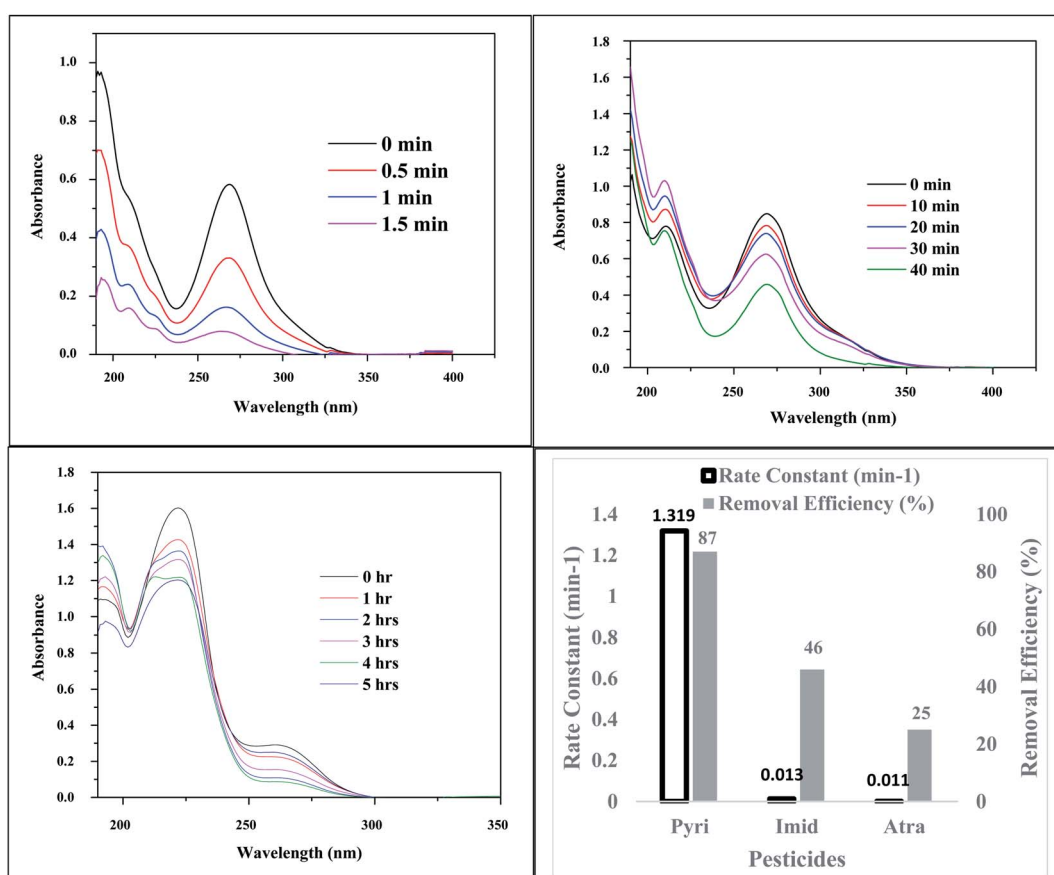


Fig. 9  $\text{Ag}_3\text{PO}_4$ -25 wt%  $\text{TiO}_2$  photodegradation of (A)  $10 \text{ mg L}^{-1}$  pyrimethanil, (B)  $10 \text{ mg L}^{-1}$  imidacloprid, (C)  $10 \text{ mg L}^{-1}$  atrazine; (D) calculated rate constants and removal efficiencies.



The first step in the photocatalytic degradation of pyrimethanil is the electrophilic substitution of one or two hydrogen atom in the pyrimethanil structure by hydroxyl radical.<sup>35</sup> Electrophilic substitution will form compounds **2** ( $m/z = 231$ ,  $t_R = 1.944$  min), **3** ( $m/z = 215$ ,  $t_R = 2.034$ ), **4** ( $m/z 215$ ,  $t_R = 2.156$  min), **5** ( $m/z = 213$ ,  $t_R = 1.653$  min), **6** ( $m/z = 177$ ,  $t_R = 1.852$  min) and **7** ( $m/z = 198$ ,  $t_R = 3.195$  min). Mono-hydroxylation of pyrimethanil will result in the formation of compound **4** with  $m/z$  215 ( $t_R = 2.034$  min). Compound **8** ( $t_R = 1.354$  min) was formed by the hydrolysis of pyrimethanil molecule with the loss of benzene ring. Aliphatic intermediate such as compound **9** ( $t_R = 5.049$  min) was also identified. Most of the intermediate compounds identified in this study were also identified by other researchers after photocatalytically

degrading pyrimethanil.<sup>36</sup> The structure of the compounds identified by LC-MS after the photocatalytic degradation of pyrimethanil are presented in Fig. 10.

It is obvious from the present study that the  $\text{Ag}_3\text{PO}_4$ – $\text{TiO}_2$  composite has an enhanced photocatalytic activity when compared to pure  $\text{Ag}_3\text{PO}_4$  and  $\text{TiO}_2$ . The photocatalytic activity of  $\text{TiO}_2$  can be enhanced by coupling it with other semiconductors. Recently published work on  $\text{Ag}_3\text{PO}_4$ – $\text{TiO}_2$  has suggested that the enhanced photocatalytic activity can be attributed to the unique band matching between  $\text{TiO}_2$  and  $\text{Ag}_3\text{PO}_4$ , inhibition of the electron hole recombination by  $\text{TiO}_2$ , and the inter semiconductor hole transfer between the valence bands of  $\text{TiO}_2$  and  $\text{Ag}_3\text{PO}_4$ .<sup>29a,33,37</sup>

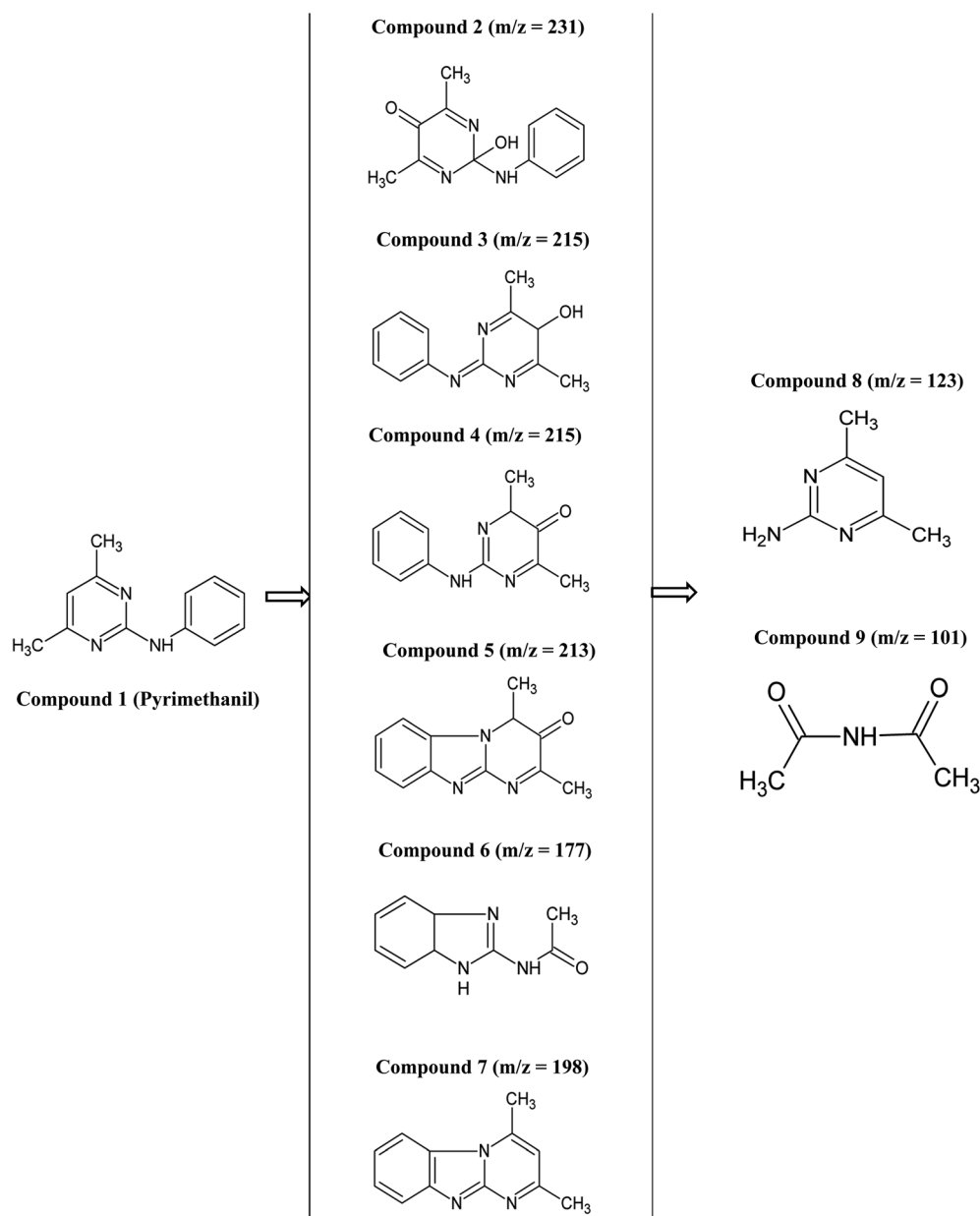


Fig. 10 The intermediate photoproducts identified by LC-MS after photodegrading pyrimethanil.



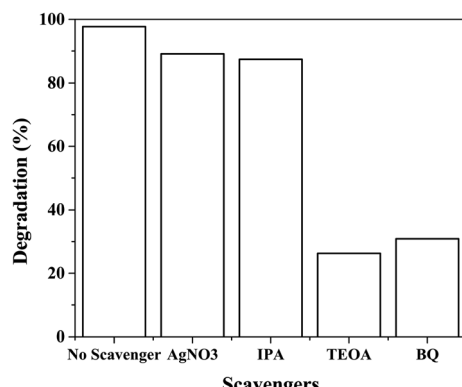


Fig. 11 Effect of scavengers on the photodegradation of rhodamine B by  $\text{Ag}_3\text{PO}_4$ -25 wt%  $\text{TiO}_2$ .

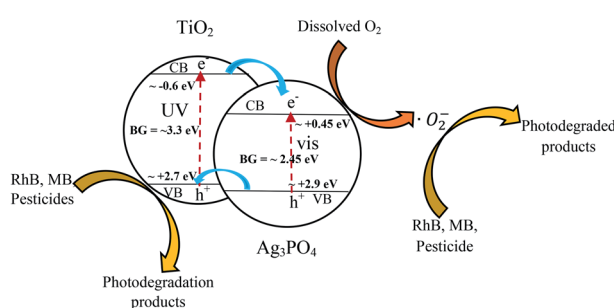


Fig. 12 Diagram for electron ( $e^-$ ) and Hole ( $h^+$ ) separation, generation of reactive oxygen species and degradation of rhodamine B (RhB), methylene blue (MB) and pesticides [BG = Band Gap].

Hydroxyl radicals, photogenerated electrons and holes, and superoxide radicals are the reactive species that are responsible for the photodegradation of organic pollutants. Benzoquinone (BQ),  $\text{AgNO}_3$ , isopropyl alcohol (IPA) and triethanolamine (TEOA) are effective scavengers for superoxide radicals ( $\cdot\text{O}_2^-$ ), photogenerated electrons ( $e^-$ ), hydroxyl radicals ( $\cdot\text{OH}$ ) and photogenerated holes ( $h^+$ ), respectively.<sup>27,30</sup> These scavengers were therefore used to examine which of the reactive species are

responsible for the degradation of rhodamine blue dye. Using  $\text{Ag}_3\text{PO}_4$ -25 wt%  $\text{TiO}_2$ , and rhodamine B solution, upon the addition of  $\text{AgNO}_3$ , IPA, TEOA and BQ, the degradation efficiency recorded reduced from 98% to 89.1%, 87.4%, 26.3% and 30.9%, respectively (Fig. 11). Therefore, photogenerated holes and superoxide radicals are the main reactive species, responsible for the photodegradation of rhodamine B dye by  $\text{Ag}_3\text{PO}_4$ -25 wt%  $\text{TiO}_2$ . This results is in agreement with the research findings of Zhang Yang *et al.*<sup>27</sup>

A possible explanation to the trend observed in this study is schematically presented in Fig. 12.

$\text{Ag}_3\text{PO}_4$  and  $\text{TiO}_2$  can be excited by visible and UV light, resulting in the generation of photo excited electrons and holes. Under UV-visible light irradiation, the electrons in the valence band of  $\text{Ag}_3\text{PO}_4$  are excited into the conduction band resulting in the generation of holes in the valence band of  $\text{Ag}_3\text{PO}_4$ . Since the valence band maxima position of  $\text{TiO}_2$  (+2.7 eV vs. NHE) is relatively higher than that of  $\text{Ag}_3\text{PO}_4$  (+2.9 eV vs. NHE),<sup>33,37</sup> the holes in the valence band of  $\text{Ag}_3\text{PO}_4$  will then be transferred into the valence band of  $\text{TiO}_2$  while the photogenerated electrons will move in the conduction band of the  $\text{Ag}_3\text{PO}_4$ . This charge transfer is possible if and only if a heterojunction is created between the  $\text{TiO}_2$  and the  $\text{Ag}_3\text{PO}_4$ . It can be seen from the SEM images in Fig. 3 that the  $\text{TiO}_2$  covered the surface of the  $\text{Ag}_3\text{PO}_4$  allowing this heterojunction to be created. The photogenerated electrons and holes are therefore separated reducing the electron-hole recombination and subsequently enhancing the photocatalytic activity. The holes generated in the valence band of the  $\text{TiO}_2$  can be used to oxidize pollutants such as dye and pesticides resulting in their degradation. In addition, the photogenerated electrons in the conduction band will react with dissolved oxygen to generate superoxide radicals. These superoxide radicals will attach pollutants and degrade them. The reactive species responsible for the degradation of organic dyes and pesticides are photogenerated holes ( $h^+$ ) and superoxide radicals ( $\cdot\text{O}_2^-$ ).

The photocatalytic activity of  $\text{Ag}_3\text{PO}_4$ - $\text{TiO}_2$  photocatalyst from this work is compared with those reported in literature. It can be seen that, the photodegradation activity of the  $\text{Ag}_3\text{PO}_4$ - $\text{TiO}_2$  synthesized from this work is high (Table 1).

Table 1 Comparison of the photocatalytic activity of  $\text{Ag}_3\text{PO}_4$ - $\text{TiO}_2$  towards the degradation of organic pollutants

Pollutant	Photocatalyst amount	Light intensity	Irradiation time	Degradation %	Ref.
Rhodamine B (200 mL, 6 mg L <sup>-1</sup> )	100 mg	300 W tungsten halogen lamp	6 min	98%	This work
Methylene blue (200 mL, 8 mg L <sup>-1</sup> )	100 mg	300 W tungsten halogen lamp	4 min	99.1%	
Rhodamine B (50 mL, 10 mg L <sup>-1</sup> )	50 mg	500 W Xe lamp	50 min	99.11%	38
Methyl orange (40 mL, 10 mg L <sup>-1</sup> )	40 mg	300 W Xe lamp	60 min	95.5%	39
Methylene blue (130 mL, 20 mg L <sup>-1</sup> )	65 mg	150 W Xe lamp	28 min	~100%	29b
Rhodamine B (100 mL, 10 mg L <sup>-1</sup> )	40 mg	300 W Xe lamp	10 min	~100%	40
Bisphenol A (120 mL, 220 $\mu\text{g/L}$ )	30 mg	100 W Xe lamp	10 min	~100%	33
Methylene blue (80 mL, 10 mM)	0.03 M	500 W xenon lamp	160 min	97.1%	41
		16 W high pressure lamp	70 min	98.1%	
Rhodamine B (100 mL, 0.02 mM)	50 mg	300 W Xe lamp	12 min	~100%	29a
Rhodamine B (100 mL, 10 mg L <sup>-1</sup> )	50 mg	500 W Xe lamp	12 min	~100%	30
Methylene blue (75 mL, 10 mg L <sup>-1</sup> )	40 mg	500 W high pressure lamp	12 min	~95%	42
Methyl orange (20 mL, 20 mg L <sup>-1</sup> )	20 mg	300 W Hg lamp	30 min	~100%	43



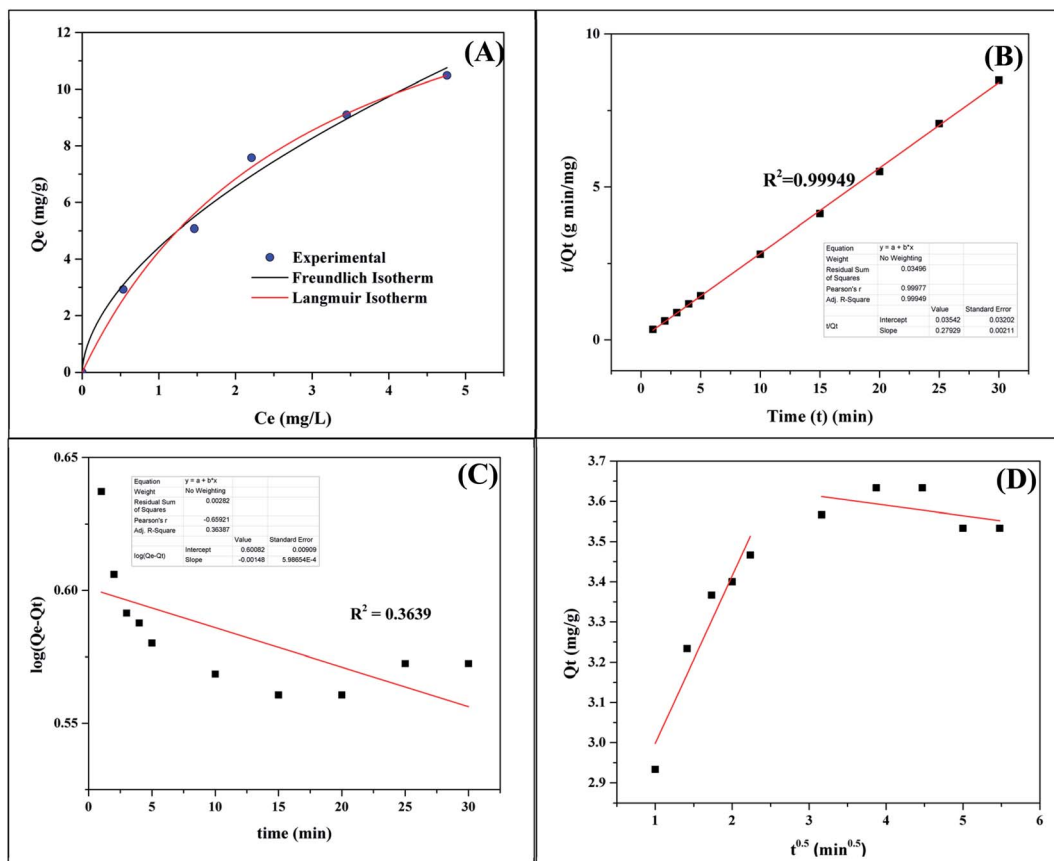


Fig. 13 (A) Langmuir and Freundlich adsorption isotherms, (B) pseudo second order (C) pseudo first order kinetics and (D) interparticle diffusion model for the adsorption of methylene blue by  $\text{Ag}_3\text{PO}_4$ -50 wt%  $\text{TiO}_2$ .

### 3.3 Adsorption equilibrium and kinetic studies

The adsorption equilibrium and kinetic studies were conducted using 200 mL of 5 mg  $\text{L}^{-1}$  methylene blue solution and 100 mg of  $\text{Ag}_3\text{PO}_4$ -50 wt%  $\text{TiO}_2$ . Fig. 13 and Table 2 contain the plots and data obtained from the adsorption studies. From Fig. 13A the amount of dye adsorbed at equilibrium ( $Q_e$ ) increased with increasing equilibrium concentration of the dye ( $C_e$ ). To obtain a better understanding of the adsorption process, the experimental data was fitted with the Langmuir and Freundlich equilibrium isotherms. The Langmuir isotherm is given as;

$$Q_e = \frac{Q_m K_L C_e}{1 + K_L C_e} \quad (1)$$

In this equation,  $C_e$  (mg  $\text{L}^{-1}$ ) is the equilibrium concentration of the dye,  $Q_e$  (mg  $\text{g}^{-1}$ ) is the amount of dye adsorbed at equilibrium,  $Q_m$  (mg  $\text{g}^{-1}$ ) is the maximum adsorption capacity corresponding to a monolayer coverage and  $K_L$  (L mg $^{-1}$ ) is the Langmuir constant. The plot of  $Q_e$  vs.  $C_e$  is presented in Fig. 13A.  $Q_m$  and  $K_L$  can be estimated from the slope and intercept of linearized Langmuir isotherm expression. The estimated  $Q_m$  and  $K_L$  are presented in Table 2. To examine the favorability or otherwise of the adsorption process, an equilibrium parameter  $R_L$  was calculated from the equation below and the values presented in Table 2.

$$R_L = \frac{1}{1 + K_L C_o} \quad (2)$$

$K_L$  (L mg $^{-1}$ ) is the Langmuir constant and  $C_o$  (mg  $\text{L}^{-1}$ ) is the initial dye concentration. The  $R_L$  value indicates adsorption process is irreversible when  $R_L$  is 0; favorable when  $R_L$  is

Table 2 Calculated adsorption isotherm and equilibrium kinetics parameters for the adsorption of methylene blue by  $\text{Ag}_3\text{PO}_4$ -50 wt%  $\text{TiO}_2$

Adsorption kinetic models	Adsorption kinetic parameters
Langmuir	$Q_m = 17.112$ (mg $\text{g}^{-1}$ ) $K_L = 0.3324$ (L mg $^{-1}$ ) $R^2 = 0.9920$
Freundlich	$R_L = 0.231-0.6$ (L mg $^{-1}$ ) $K_F = 4.4181$ (mg $\text{g}^{-1}$ (mg $\text{L}^{-1}$ ) $^{1/n}$ ) $n = 1.7531$ $R^2 = 0.9888$
Pseudo first order	$Q_e = 3.9886$ (mg $\text{g}^{-1}$ ) $K_1 = 0.00341$ (min $^{-1}$ ) $R^2 = 0.3639$
Pseudo second order	$Q_e = 3.5804$ (mg $\text{g}^{-1}$ ) $K_2 = 2.2036$ (g mg $^{-1}$ min $^{-1}$ ) $R^2 = 0.9995$
Interparticle diffusion model	$K_P = 2.5812$ (mg $\text{g}^{-1}$ min $^{-1/2}$ ) $R^2 = 0.9189$

between 0 and 1; linear when  $R_L$  is 1 and unfavorable when  $R_L$  is greater than 1. The maximum monolayer adsorption capacity ( $Q_m$ ) and the equilibrium parameter ( $R_L$ ) of the  $\text{Ag}_3\text{PO}_4$ -50 wt%  $\text{TiO}_2$  were calculated to be 17.112 mg g<sup>-1</sup> and 0.231–0.600, respectively. These values imply that the surface of the  $\text{Ag}_3\text{PO}_4$ -50 wt%  $\text{TiO}_2$  is homogenous and was covered with a monolayer methylene blue dye. In addition, the adsorption of methylene blue by  $\text{Ag}_3\text{PO}_4$ -50 wt%  $\text{TiO}_2$  was favorable.

In addition to the Langmuir equilibrium model, the adsorption data was fitted with the Freundlich equation. The Freundlich equation is presented below;

$$Q_e = K_F C_e^{1/n} \quad (3)$$

$Q_e$  (mg g<sup>-1</sup>) is the amount of dye adsorbed on  $\text{Ag}_3\text{PO}_4$ -50 wt%  $\text{TiO}_2$  at equilibrium,  $C_e$  is the equilibrium concentration of the dye in solution,  $K_F$  (mg g<sup>-1</sup>(mg L<sup>-1</sup>)<sup>1/n</sup>) and  $1/n$  are the Freundlich constants related to the adsorption capacity and the adsorption intensity, respectively. Higher values of  $K_F$  indicate higher affinity for adsorption and the values of  $1/n$  lie between  $0.1 < 1/n < 1$ , indicating favorable adsorption.<sup>44</sup> The Freundlich constants were calculated from the linearized Freundlich isotherm expression and presented in Table 2. The value of  $1/n$  is less than 1 indicating favorable adsorption process. The  $K_F$  and a correlation coefficient were estimated as 4.4181 mg g<sup>-1</sup> (mg L<sup>-1</sup>)<sup>1/n</sup> and 0.9888, respectively. Since the correlation coefficient for both the Langmuir and Freundlich model were greater than 0.95, the adsorption process may have followed both models. It is however likely the adsorption process followed the Langmuir isotherm model since it had a relatively higher correlation coefficient when compared to Freundlich isotherm.

The mechanism and rate controlling step of the entire adsorption process was examined using the following adsorption kinetic models; pseudo-first order, pseudo-second order and intra-particle diffusion models. The pseudo-first order equation is presented below;

$$\log(Q_e - Q_t) = \log Q_e - \frac{K_1}{2.303} t \quad (4)$$

$Q_e$  and  $Q_t$  (mg g<sup>-1</sup>) are the amount of the dye adsorbed at equilibrium and at time  $t$  (min), respectively.  $K_1$  (min<sup>-1</sup>) is the pseudo-first order rate constant. The parameters  $K_1$  and  $Q_e$  were estimated from Fig. 13C and presented in Table 2. The correlation coefficient obtained is low ( $R^2 = 0.3639$ ). This suggests that the pseudo-first order kinetic model is not suitable to describe the adsorption process.

The adsorption kinetics was also investigated using pseudo-second order kinetic model presented below;

$$\frac{t}{Q_t} = \frac{1}{K_2 Q_e} + \frac{t}{Q_e} \quad (5)$$

$K_2$  (g mg<sup>-1</sup> min<sup>-1</sup>) is the pseudo-second order rate constant.  $Q_e$  and  $Q_t$  (mg g<sup>-1</sup>) are the amount of dye adsorbed at equilibrium and at time  $t$  (min), respectively.  $Q_e$  and  $K_2$  were calculated from Fig. 13B. The high correlation coefficient of 0.9995 suggests that the adsorption process follows a pseudo-second order adsorption kinetics process.

The Langmuir adsorption isotherm confirm the monolayer adsorption of methylene blue onto the surface of the  $\text{Ag}_3\text{PO}_4$ -50 wt%  $\text{TiO}_2$ . The dye molecules were probably transported from the dye solution to the  $\text{Ag}_3\text{PO}_4$ -50 wt%  $\text{TiO}_2$ . The possibility of intra-particle diffusion was therefore examined using the intra-particle diffusion model<sup>45</sup> presented below;

$$Q_t = K_p t^{1/2} + C \quad (6)$$

$Q_t$  (mg g<sup>-1</sup>) is the amount of methylene blue dye adsorbed at time  $t$  (min),  $C$  is the intercept and  $K_p$  (mg g<sup>-1</sup> min<sup>-1</sup>) is the intra-particle diffusion rate constant.  $K_p$  was estimated from Fig. 13D and presented in Table 2. The plot in Fig. 13D shows a double straight line. The initial stage represents the transportation of methylene blue to the external surface of the  $\text{Ag}_3\text{PO}_4$ -50 wt%  $\text{TiO}_2$  through film diffusion within a very short time. The first linear part can be due to the entry of methylene blue molecules into the  $\text{Ag}_3\text{PO}_4$ -50 wt%  $\text{TiO}_2$  by intra-particle diffusion.<sup>46</sup> The final equilibrium stage is represented by the second linear portion of Fig. 13D.

The results presented in this article revealed that  $\text{TiO}_2$ - $\text{Ag}_3\text{PO}_4$  has the potential of removing water pollutants through adsorption and photocatalysis.  $\text{TiO}_2$ - $\text{Ag}_3\text{PO}_4$  therefore has a potential application in the development of water treatment technologies.

## 4 Conclusion

In this study,  $\text{TiO}_2$  semiconductor was coupled with  $\text{Ag}_3\text{PO}_4$ . SEM images of the as-prepared  $\text{TiO}_2$ - $\text{Ag}_3\text{PO}_4$  showed a covering of the  $\text{Ag}_3\text{PO}_4$  surface by  $\text{TiO}_2$  creating a heterojunction between coupled semiconductors. DRS analysis and optical band gap estimation revealed two absorption thresholds corresponding to  $\text{TiO}_2$  and  $\text{Ag}_3\text{PO}_4$ .  $\text{TiO}_2$ - $\text{Ag}_3\text{PO}_4$  showed strong photocatalytic activity for rhodamine B, methylene blue, pyrimethanil, imidacloprid and atrazine. LC-MS analysis of the photodegraded pyrimethanil resulted in the identification of hydroxylated and aliphatic derivatives of pyrimethanil. The photocatalytic activity was dependent on the weight percent of the  $\text{TiO}_2$  used in the synthesis with 25 wt%  $\text{TiO}_2$  recording the highest photocatalytic removal efficiency and rate constant. The synergy between the  $\text{TiO}_2$  and  $\text{Ag}_3\text{PO}_4$  semiconductors was attributed to the good band gap matching that resulted in the efficient separation of charges which in turn led to a suppression of the electron-hole recombination. The  $\text{TiO}_2$ - $\text{Ag}_3\text{PO}_4$  showed strong adsorption towards methylene blue dye and the adsorption equilibrium isotherm and kinetics followed the Freundlich and Langmuir isotherms, and pseudo second order rate kinetics, respectively.  $\text{TiO}_2$ - $\text{Ag}_3\text{PO}_4$  therefore removes the pollutants by both photocatalytic and adsorption process. The results from this study showed the potential application of  $\text{TiO}_2$ - $\text{Ag}_3\text{PO}_4$  in water treatment technologies.

## Conflicts of interest

There is no conflict to declare.



## Acknowledgements

This work was financially supported through Commonwealth Academic Fellowship funded by the UK Government.

## References

- 1 (a) I. K. Konstantinou and T. A. Albanis, Photocatalytic transformation of pesticides in aqueous titanium dioxide suspensions using artificial and solar light: intermediates and degradation pathways, *Appl. Catal., B*, 2003, **42**(4), 319–335; (b) N. Daneshvar, D. Salari and A. Khataee, Photocatalytic degradation of azo dye acid red 14 in water on ZnO as an alternative catalyst to TiO<sub>2</sub>, *J. Photochem. Photobiol., A*, 2004, **162**(2–3), 317–322; (c) S. E. Bailey, T. J. Olin, R. M. Bricka and D. D. Adrian, A review of potentially low-cost sorbents for heavy metals, *Water Res.*, 1999, **33**(11), 2469–2479; (d) S. D. Kim, J. Cho, I. S. Kim, B. J. Vanderford and S. A. Snyder, Occurrence and removal of pharmaceuticals and endocrine disruptors in South Korean surface, drinking, and waste waters, *Water Res.*, 2007, **41**(5), 1013–1021; (e) E. Nyankson and R. Kumar, Removal of water-soluble dyes and pharmaceutical wastes by combining the photocatalytic properties of Ag<sub>3</sub>PO<sub>4</sub> with the adsorption properties of halloysite nanotubes, *Materials Today Advances*, 2019, **4**, 100025.
- 2 I. K. Konstantinou and T. A. Albanis, TiO<sub>2</sub>-assisted photocatalytic degradation of azo dyes in aqueous solution: kinetic and mechanistic investigations: A review, *Appl. Catal., B*, 2004, **49**(1), 1–14.
- 3 C. Ràfols and D. Barceló, Determination of mono-and disulphonated azo dyes by liquid chromatography-atmospheric pressure ionization mass spectrometry, *J. Chromatogr. A*, 1997, **777**(1), 177–192.
- 4 L. Lhomme, S. Brosillon and D. Wolbert, Photocatalytic degradation of pesticides in pure water and a commercial agricultural solution on TiO<sub>2</sub> coated media, *Chemosphere*, 2008, **70**(3), 381–386.
- 5 (a) J. E. Barbash, G. P. Thelin, D. W. Kolpin and R. J. Gilliom, Major herbicides in ground water, *J. Environ. Qual.*, 2001, **30**(3), 831–845; (b) J. Fenoll, P. Flores, P. Hellín, C. M. Martínez and S. Navarro, Photodegradation of eight miscellaneous pesticides in drinking water after treatment with semiconductor materials under sunlight at pilot plant scale, *Chem. Eng. J.*, 2012, **204**, 54–64.
- 6 (a) Y. Shen, Q. Xu, R. Wei, J. Ma and Y. Wang, Mechanism and dynamic study of reactive red X-3B dye degradation by ultrasonic-assisted ozone oxidation process, *Ultrason. Sonochem.*, 2017, **38**, 681–692; (b) A. Tawk, M. Deborde, J. Labanowski, S. Thibaudeau and H. Gallard, Transformation of the B-triketone pesticides tembotrione and sulcotrione by reactions with ozone: Kinetic study, transformation products, toxicity and biodegradability, *Ozone: Sci. Eng.*, 2017, **39**(1), 3–13; (c) A. Derylo-Marczewska, M. Blachnio, A. W. Marczewski, A. Swiatkowski and B. Buczek, Adsorption of chlorophenoxy pesticides on activated carbon with gradually removed external particle layers, *Chem. Eng. J.*, 2017, **308**, 408–418; (d) M. R. Sohrabi, A. Khavaran, S. Shariati and S. Shariati, Removal of Carmoisine edible dye by Fenton and photo Fenton processes using Taguchi orthogonal array design, *Arabian J. Chem.*, 2017, **10**, S3523–S3531.
- 7 E. Forgacs, T. Cserhati and G. Oros, Removal of synthetic dyes from wastewaters: a review, *Environ. Int.*, 2004, **30**(7), 953–971.
- 8 (a) M. Cruz, C. Gomez, C. J. Duran-Valle, L. M. Pastrana-Martínez, J. L. Faria, A. M. Silva, M. Faraldo and A. Bahamonde, Bare TiO<sub>2</sub> and graphene oxide TiO<sub>2</sub> photocatalysts on the degradation of selected pesticides and influence of the water matrix, *Appl. Surf. Sci.*, 2017, **416**, 1013–1021; (b) S.-F. Yang, C.-G. Niu, D.-W. Huang, H. Zhang, C. Liang and G.-M. Zeng, SrTiO<sub>3</sub> nanocubes decorated with Ag/AgCl nanoparticles as photocatalysts with enhanced visible-light photocatalytic activity towards the degradation of dyes, phenol and bisphenol A, *Environ. Sci.: Nano*, 2017, **4**(3), 585–595; (c) H. Agbe, E. Nyankson, N. Raza, D. Dodoo-Arhin, A. Chauhan, G. Osei, V. Kumar and K.-H. Kim, Recent advances in photoinduced catalysis for water splitting and environmental applications, *J. Ind. Eng. Chem.*, 2019, **72**, 31–49.
- 8d E. Nyankson, B. Agyei-Tuffour, J. Adjasioo, A. Ebenezer, D. Dodoo-Arhin, A. Yaya, B. Mensah and J. K. Efaví, Synthesis and application of Fe-doped TiO<sub>2</sub>-halloysite nanotubes composite and their potential application in water treatment, *Adv. Mater. Sci. Eng.*, 2019, 2019;
- 9 B. Agyei-Tuffour, S. Gbogbo, D. Dodoo-Arhin, L. N. Damoah, J. K. Efaví, A. Yaya and E. Nyankson, Photocatalytic degradation of fractionated crude oil: potential application in oil spill remediation, *Cogent Engineering*, 2020, **7**(1), 1744944.
- 10 D. Dodoo-Arhin, E. Bowen-Dodoo, B. Agyei-Tuffour, E. Nyankson, J. D. Obayemi, A. A. Salifu, A. Yaya, H. Agbe and W. O. Soboyejo, Modified nanostructured titania photocatalysts for aquatic disinfection applications, *Mater. Today: Proc.*, 2020, **38**, 1183–1190.
- 11 I. Oller, W. Gernjak, M. Maldonado, L. Pérez-Estrada, J. Sánchez-Pérez and S. Malato, Solar photocatalytic degradation of some hazardous water-soluble pesticides at pilot-plant scale, *J. Hazard. Mater.*, 2006, **138**(3), 507–517.
- 12 (a) A. Kumar, K. Kumar and V. Krishnan, Sunlight driven methanol oxidation by anisotropic plasmonic Au nanostructures supported on amorphous titania: Influence of morphology on photocatalytic activity, *Mater. Lett.*, 2019, **245**, 45–48; (b) A. Kumar, V. Sharma, S. Kumar, A. Kumar and V. Krishnan, Towards utilization of full solar light spectrum using green plasmonic Au-TiO<sub>x</sub> photocatalyst at ambient conditions, *Surf. Interfaces*, 2018, **11**, 98–106.
- 13 Z. Lu, L. Zeng, W. Song, Z. Qin, D. Zeng and C. Xie, In situ synthesis of C-TiO<sub>2</sub>/g-C<sub>3</sub>N<sub>4</sub> heterojunction nanocomposite as highly visible light active photocatalyst originated from effective interfacial charge transfer, *Appl. Catal., B*, 2017, **202**, 489–499.
- 14 M. Ismael, E. Elhaddad, D. H. Taffa and M. Wark, Synthesis of Phase Pure Hexagonal YFeO<sub>3</sub> Perovskite as Efficient Visible Light Active Photocatalyst, *Catalysts*, 2017, **7**(11), 326.





15 T. Bora, P. Sathe, K. Laxman, S. Dobretsov and J. Dutta, Defect engineered visible light active ZnO nanorods for photocatalytic treatment of water, *Catal. Today*, 2017, **284**, 11–18.

16 S. Harish, J. Archana, M. Sabarinathan, M. Navaneethan, K. Nisha, S. Ponnusamy, C. Muthamizhchelvan, H. Ikeda, D. Aswal and Y. Hayakawa, Controlled structural and compositional characteristic of visible light active ZnO/CuO photocatalyst for the degradation of organic pollutant, *Appl. Surf. Sci.*, 2017, **418**, 103–112.

17 Y.-H. Li, J.-Y. Li and Y.-J. Xu, Bimetallic Nanoparticles as Cocatalysts for Versatile Photoredox Catalysis, *Surf. Interfaces*, 2020, 100047.

18 (a) F. Zhang, Y.-H. Li, J.-Y. Li, Z.-R. Tang and Y.-J. Xu, 3D graphene-based gel photocatalysts for environmental pollutants degradation, *Environ. Pollut.*, 2019, **253**, 365–376; (b) K.-Q. Lu, X. Xin, N. Zhang, Z.-R. Tang and Y.-J. Xu, Photoredox catalysis over graphene aerogel-supported composites, *J. Mater. Chem. A*, 2018, **6**(11), 4590–4604.

19 (a) Z. Yi, J. Ye, N. Kikugawa, T. Kako, S. Ouyang, H. Stuart-Williams, H. Yang, J. Cao, W. Luo and Z. Li, An orthophosphate semiconductor with photooxidation properties under visible-light irradiation, *Nat. Mater.*, 2010, **9**(7), 559; (b) E. Nyankson, R. Amedalor, G. Chandrabose, M. Coto, S. Krishnamurthy and R. V. Kumar, Microwave-and Formaldehyde-Assisted Synthesis of Ag–Ag<sub>3</sub>PO<sub>4</sub> with Enhanced Photocatalytic Activity for the Degradation of Rhodamine B Dye and Crude Oil Fractions, *ACS Omega*, 2020, **5**(23), 13641–13655.

20 Y. Bi, S. Ouyang, J. Cao and J. Ye, Facile synthesis of rhombic dodecahedral AgX/Ag<sub>3</sub>PO<sub>4</sub> (X= Cl, Br, I) heterocrystals with enhanced photocatalytic properties and stabilities, *Phys. Chem. Chem. Phys.*, 2011, **13**(21), 10071–10075.

21 Z. Chen, W. Wang, Z. Zhang and X. Fang, High-efficiency visible-light-driven Ag<sub>3</sub>PO<sub>4</sub>/AgI photocatalysts: Z-scheme photocatalytic mechanism for their enhanced photocatalytic activity, *J. Phys. Chem. C*, 2013, **117**(38), 19346–19352.

22 H. Katsumata, T. Sakai, T. Suzuki and S. Kaneko, Highly efficient photocatalytic activity of g-C<sub>3</sub>N<sub>4</sub>/Ag<sub>3</sub>PO<sub>4</sub> hybrid photocatalysts through Z-scheme photocatalytic mechanism under visible light, *Ind. Eng. Chem. Res.*, 2014, **53**(19), 8018–8025.

23 H. Zhang, H. Huang, H. Ming, H. Li, L. Zhang, Y. Liu and Z. Kang, Carbon quantum dots/Ag<sub>3</sub>PO<sub>4</sub> complex photocatalysts with enhanced photocatalytic activity and stability under visible light, *J. Mater. Chem.*, 2012, **22**(21), 10501–10506.

24 X. Guan and L. Guo, Cocatalytic effect of SrTiO<sub>3</sub> on Ag<sub>3</sub>PO<sub>4</sub> toward enhanced photocatalytic water oxidation, *ACS Catal.*, 2014, **4**(9), 3020–3026.

25 D. Dodoo-Arhin, F. P. Buabeng, J. M. Mwabora, P. N. Amaniampong, H. Agbe, E. Nyankson, D. O. Obada and N. Y. Asiedu, The effect of titanium dioxide synthesis technique and its photocatalytic degradation of organic dye pollutants, *Heliyon*, 2018, **4**(7), e00681.

26 (a) L. Zhang, H. Zhang, H. Huang, Y. Liu and Z. Kang, Ag<sub>3</sub>PO<sub>4</sub>/SnO<sub>2</sub> semiconductor nanocomposites with enhanced photocatalytic activity and stability, *New J. Chem.*, 2012, **36**(8), 1541–1544; (b) Y. Jia, Y. Ma, L. Zhu, J. Dong and Y. Lin, Efficient visible-light-responsive photocatalyst: hybrid TiO<sub>2</sub>-Ag<sub>3</sub>PO<sub>4</sub> nanorods, *Chem. Phys.*, 2019, **521**, 1–4.

27 Y. Zhang, G. Duoerkun, Z. Shi, W. Cao, T. Liu, J. Liu, L. Zhang, M. Li and Z. Chen, Construction of TiO<sub>2</sub>/Ag<sub>3</sub>PO<sub>4</sub> nanojunctions on carbon fiber cloth for photocatalytically removing various organic pollutants in static or flowing wastewater, *J. Colloid Interface Sci.*, 2020, **571**, 213–221.

28 M. Al Kausor and D. Chakrabortty, Facile fabrication of N-TiO<sub>2</sub>/Ag<sub>3</sub>PO<sub>4</sub>@GO nanocomposite toward photodegradation of organic dye under visible light, *Inorg. Chem. Commun.*, 2020, **116**, 107907.

29 (a) F.-M. Zhao, L. Pan, S. Wang, Q. Deng, J.-J. Zou, L. Wang and X. Zhang, Ag<sub>3</sub>PO<sub>4</sub>/TiO<sub>2</sub> composite for efficient photodegradation of organic pollutants under visible light, *Appl. Surf. Sci.*, 2014, **317**, 833–838; (b) Y. Li, L. Yu, N. Li, W. Yan and X. Li, Heterostructures of Ag<sub>3</sub>PO<sub>4</sub>/TiO<sub>2</sub> mesoporous spheres with highly efficient visible light photocatalytic activity, *J. Colloid Interface Sci.*, 2015, **450**, 246–253; (c) A. Hamrouni, H. Azzouzi, A. Rayes, L. Palmisano, R. Ceccato and F. Parrino, Enhanced solar light photocatalytic activity of ag doped TiO<sub>2</sub>-Ag<sub>3</sub>PO<sub>4</sub> composites, *Nanomaterials*, 2020, **10**(4), 795.

30 L. Yang, W. Duan, H. Jiang, S. Luo and Y. Luo, Mesoporous TiO<sub>2</sub>@Ag<sub>3</sub>PO<sub>4</sub> photocatalyst with high adsorbility and enhanced photocatalytic activity under visible light, *Mater. Res. Bull.*, 2015, **70**, 129–136.

31 C. Li, P. Zhang, R. Lv, J. Lu, T. Wang, S. Wang, H. Wang and J. Gong, Selective deposition of Ag<sub>3</sub>PO<sub>4</sub> on monoclinic BiVO<sub>4</sub> (040) for highly efficient photocatalysis, *Small*, 2013, **9**(23), 3951–3956.

32 R. Zanella, S. Giorgio, C. R. Henry and C. Louis, Alternative methods for the preparation of gold nanoparticles supported on TiO<sub>2</sub>, *J. Phys. Chem. B*, 2002, **106**(31), 7634–7642.

33 M. E. Taheri, A. Petala, Z. Frontistis, D. Mantzavinos and D. I. Kondarides, Fast photocatalytic degradation of bisphenol A by Ag<sub>3</sub>PO<sub>4</sub>/TiO<sub>2</sub> composites under solar radiation, *Catal. Today*, 2017, **280**, 99–107.

34 R. López and R. Gómez, Band-gap energy estimation from diffuse reflectance measurements on sol-gel and commercial TiO<sub>2</sub>: a comparative study, *J. Sol-Gel Sci. Technol.*, 2012, **61**(1), 1–7.

35 (a) C. Sirtori, A. Zapata, S. Malato and A. Agüera, Formation of chlorinated by-products during photo-Fenton degradation of pyrimethanil under saline conditions. Influence on toxicity and biodegradability, *J. Hazard. Mater.*, 2012, **217–218**, 217–223; (b) A. Kinani, A. Rifai, S. Bourcier, F. Jaber and S. Bouchonnet, Structural characterization of photoproducts of pyrimethanil, *J. Mass Spectrom.*, 2013, **48**(8), 983–987.

36 A. Agüera, E. Almansa, A. Tejedor, A. R. Fernandez-Alba, S. Malato and M. I. Maldonado, Photocatalytic pilot scale degradation study of pyrimethanil and of its main

degradation products in waters by means of solid-phase extraction followed by gas and liquid chromatography with mass spectrometry detection, *Environ. Sci. Technol.*, 2000, **34**(8), 1563–1571.

37 S. B. Rawal, S. Do Sung and W. I. Lee, Novel Ag<sub>3</sub>PO<sub>4</sub>/TiO<sub>2</sub> composites for efficient decomposition of gaseous 2-propanol under visible-light irradiation, *Catal. Commun.*, 2012, **17**, 131–135.

38 P. Wang, Y. Li, Z. Liu, J. Chen, Y. Wu, M. Guo and P. Na, In-situ deposition of Ag<sub>3</sub>PO<sub>4</sub> on TiO<sub>2</sub> nanosheets dominated by (001) facets for enhanced photocatalytic activities and recyclability, *Ceram. Int.*, 2017, **43**(15), 11588–11595.

39 H. Liu, D. Li, X. Yang and H. Li, Fabrication and characterization of Ag<sub>3</sub>PO<sub>4</sub>/TiO<sub>2</sub> heterostructure with improved visible-light photocatalytic activity for the degradation of methyl orange and sterilization of *E. coli*, *Mater. Technol.*, 2019, **34**(4), 192–203.

40 J. Xie, Y. Yang, H. He, D. Cheng, M. Mao, Q. Jiang, L. Song and J. Xiong, Facile synthesis of hierarchical Ag<sub>3</sub>PO<sub>4</sub>/TiO<sub>2</sub> nanofiber heterostructures with highly enhanced visible light photocatalytic properties, *Appl. Surf. Sci.*, 2015, **355**, 921–929.

41 C. Tang, E. Liu, J. Fan, X. Hu, L. Kang and J. Wan, Heterostructured Ag<sub>3</sub>PO<sub>4</sub>/TiO<sub>2</sub> nano-sheet film with high efficiency for photodegradation of methylene blue, *Ceram. Int.*, 2014, **40**(10), 15447–15453.

42 X. Ma, H. Li, Y. Wang, H. Li, B. Liu, S. Yin and T. Sato, Substantial change in phenomenon of “self-corrosion” on Ag<sub>3</sub>PO<sub>4</sub>/TiO<sub>2</sub> compound photocatalyst, *Appl. Catal., B*, 2014, **158**, 314–320.

43 R. Liu, P. Hu and S. Chen, Photocatalytic activity of Ag<sub>3</sub>PO<sub>4</sub> nanoparticle/TiO<sub>2</sub> nanobelト heterostructures, *Appl. Surf. Sci.*, 2012, **258**(24), 9805–9809.

44 (a) V. K. Gupta, C. Jain, I. Ali, S. Chandra and S. Agarwal, Removal of lindane and malathion from wastewater using bagasse fly ash—a sugar industry waste, *Water Res.*, 2002, **36**(10), 2483–2490; (b) A. S. Özcan, B. Erdem and A. Özcan, Adsorption of Acid Blue 193 from aqueous solutions onto Na-bentonite and DTMA-bentonite, *J. Colloid Interface Sci.*, 2004, **280**(1), 44–54.

45 M. Doğan, M. Alkan, A. Türkyılmaz and Y. Özdemir, Kinetics and mechanism of removal of methylene blue by adsorption onto perlite, *J. Hazard. Mater.*, 2004, **109**(1–3), 141–148.

46 P. Luo, Y. Zhao, B. Zhang, J. Liu, Y. Yang and J. Liu, Study on the adsorption of Neutral Red from aqueous solution onto halloysite nanotubes, *Water Res.*, 2010, **44**(5), 1489–1497.

